A Wideband Self-Consistent Disk-Averaged Spectrum of Jupiter Near 30 GHz and Its Implications for NH_3 Saturation in the Upper Troposphere

Ramsey Karim, David DeBoer, Imke de Pater, Garrett Keating

September 18, 2017

Abstract

We present a new set of CARMA measurements of Jupiter's thermal emission in the microwave, near the 1.3 cm ammonia (NH_3) absorption band, which we use to investigate ammonia abundance in the upper troposphere, near $0.3 < P < 2$ bar, based on radiative transfer modeling. We find ammonia to be present at over half the nominal value below the $P \sim 0.8$ bar NH_3 cloud layer, corresponding to a new deep ($P \sim 8$ bar) atmosphere fractional abundance of 2.4×10^{-4}. This conclusion is not extended past $P = 8$ bar, since our measurements have no sensitivity and the result would contradict Galileo probe results. We find the NH_3 cloud-forming region between $0.3 < P < 0.8$ bar to be globally subsaturated by 55% on average, in accordance with the result in Gibson et al. 2005. While these data are not very sensitive to the region above the cloud layer, we are able to set an upper limit of 2.4×10^{-7} on the abudance here, although both our fitting process and the Clausius-Clapeyron equation of state suggest something closer to $\sim 2 \times 10^{-8}$. All three results agree that NH_3 abundance is a factor of 2 lower than suggested by Galileo probe results above $P < 2$ bar, a conclusion consistent with the Gibson et al. 2005 result as well as the ground-based radio models discussed in de Pater et al. 2001.

1   Introduction

Microwave observations of Jupiter's atmosphere are generally dominated by pressure-broadened spectral features of ammonia gas in the troposphere. The most notable feature in this region of the gas giant's thermal spectrum is the 1.3 cm NH_3 inversion/absorption band, first reported as a single, broad line by Law and Staelin 1968 and declared by Klein and Gulkis 1978 to be a "diagnostic of the pressure and temperature profiles in the cloud-forming region of the Jovian atmosphere." As we continue to sample Jupiter's thermal spectrum around this band, we can better characterize the shape of this spectral feature, which, through proper analysis, provides us with a deeper understanding of the planet's vertical structure and improves Jupiter's usefulness as a radio calibrator.

Decades of disk-averaged, and more recently, spatially resolved, observations as well as in situ probe measurements have contributed to understanding the planet's atmospheric structure. Ammonia's presence in the jovian atmosphere was first noted by Wildt 1937 using evidence from the visible spectrum, but it was not until the 1950s-60s that the radio spectrum was explored more thoroughly in order to derive a consistent ammonia abundance. This mid-to-late 20th century investigation of Jupiter's microwave spectrum suggested a relatively straightforward model involving an adiabatic atmosphere with roughly solar NH_3 abundance in the deep atmosphere, which is considered to be well-mixed. The detailed radiative transfer analysis presented in de Pater and Massie 1985 agrees, stating solar NH_3 abundance to within a factor of 2 until $P < 0.5$ bar, above which NH_3 drops by $\sim 10^3$. This depletion is consistent with NH_3 condensation following the saturated vapor curve.

Modern efforts to uncover more about the planets vertical structure have also raised new questions (de Pater et al. 2005). The Galileo probe mission of the 1990s presented *in situ* measurements of NH_3 abundance that arguably conflict with ground-based radio observational models, creating what de Pater et al. 2005 calls the "Galileo Ground-based Microwave Paradox." Probe measurements suggest that NH_3 abundance should be nearly $4\times$ solar [1]. Given the previously accepted model, this result was jarring.

---

[1] We designate a solar model based on the most recent proto-solar elemental abundance estimates (Asplund et al. 2009). N/H2 is taken to be 1.48×10^{-4}. Henceforth, the solar NH_3 abundance value is 1.28×10^{-4}.

The paradox demands further investigation in both observational categories.

This work focuses on the ground-based and disk-averaged case and aims to fine-tune the model referred to by de Pater et al. 2001 as the "Radio Model" of NH_3 abundance based on this type of observation. Contemporary microwave observations include the 20-24 GHz cluster by Klein and Gulkis 1978 and the 20-90 GHz span of 5 measurements made using the Wilkinson Microwave Anisotropy Probe (WMAP) presented in Page et al. 2003 and updated in Weiland et al. 2011. Gibson et al. 2003 provides a single, well-calibrated point at 28.5 GHz while Gibson et al. 2005 (henceforth JG) corrects and discusses all three of these sets, concluding that NH_3 is globally subsolar between $0.6 < P < 2$ bar and subsaturated by more than 50% between $0.4 < P < 0.6$ bar. Measurements presented more recently by de Pater et al. 2016 fill in the lower-frequency side, from about 5 to 20 GHz. Each of these contemporary measurements contributes heavily to the current radio model and our understanding of the planet's vertical structure; the multi-measurement sets paint the general line shape in broad strokes across tens of GHz, while the point from Gibson et al. 2003 confidently pins down an absolute brightness temperature. What is not yet seen in this spectrum is a tightly packed cluster of self-consistent measurements indicating a local spectral slope. We wish to present this missing piece with our contribution of 15 thermal brightness measurements spanning 27-35 GHz, a short frequency regime relative to the decades spanned by extant sets.

de Pater et al. 2016 applies a model that takes NH_3 abundance to be $4.5\times$ solar (5.72×10^{-4}) in the deep atmosphere, inspired by the Galileo results, and then follows the saturated vapor curve within and above the cloud layers. This model, described in more detail in Section 3, is henceforth referred to as the "nominal" model and serves as the base model for this work. From this point, our radiative transfer analysis of the available measurements, described below, should tune this nominal model into a Radio Model of improved accuracy.

2 Data

One of the last studies conducted with the Combined Array for Research in Millimeter-wave Astronomy (CARMA) was a CO power spectrum survey which aimed to measure the CO(1-0) transition in redshift ~ 3 galaxies (Keating et al. 2015; Keating et al. 2016, hereafter referred to as COPSS). The compact, 8-element Sunyaev-Zel'dovich Array (SZA) subset of CARMA was used to take various field scans between 27-35 GHz, where such a redshifted $\lambda_0 = 115$ GHz line would lie. COPSS used Mars as the primary calibrator, but recorded secondary calibration scans of Jupiter for redundancy. It is these observations, taken between December 2014 and the array's decommission in April 2015, that are used in this work.

The SZA is a set of eight 3.5 m elements sensitive to left circularly polarized radiation. Since it does not resolve the planet, the synthesized beam from this array is sufficient for measurements of Jupiter's total flux density. All further analysis is thus restricted to the case of the atmosphere averaged across the projected observable surface of the planet at the time of the observation, which, when averaged over time, presents a reasonable disk-averaged measurement of the planet's flux density. The calibration data from COPSS comprise flux densities spanning 15 channels from 27-35 GHz (0.8 to 1.1 cm) and 100 days between December 2014 and April 2015. Error estimates accompanying the data have typical values of ~ 0.01 Jy and account only for thermal error. Uncertainty in the absolute flux calibration is preliminarily estimated at $< 5\%$ according to COPSS, but we present our own thorough investigation in Section 2.1.1. CARMA in its entirety is a fairly spectrally stable instrument, so we expect relative uncertainty to be somewhat smaller than absolute uncertainty; this too will be discussed shortly.

2.1 Flux Measurement Reduction

Reduction of these data, for each channel, converts a time series of flux densities to a single brightness temperature. The process also isolates and corrects for a variety of systematics throughout the process. The result is 15 time- and disk-averaged measurements of Jupiter's brightness on the short wave side of the 1.3 cm ammonia absorption band.

The effects of Jupiter's distance from Earth during the observational period are removed through distance normalization to the nominal value of 4.04 AU, "flattening" each channel's measurement as is made evident between the two panels in Figure 1. This step facilitates examination of antenna gain error, indicated by the variance in the normalized points as well as the cross-channel behavior during individual observations. Jackknife testing, discussed in more detail in Section 2.3, reveals an additional artifact at this stage. The series of flux densities for each channel show positive linear correlation with Jupiter's elevation in the sky at the time of observation, indicating some potential issue with airmass calibration
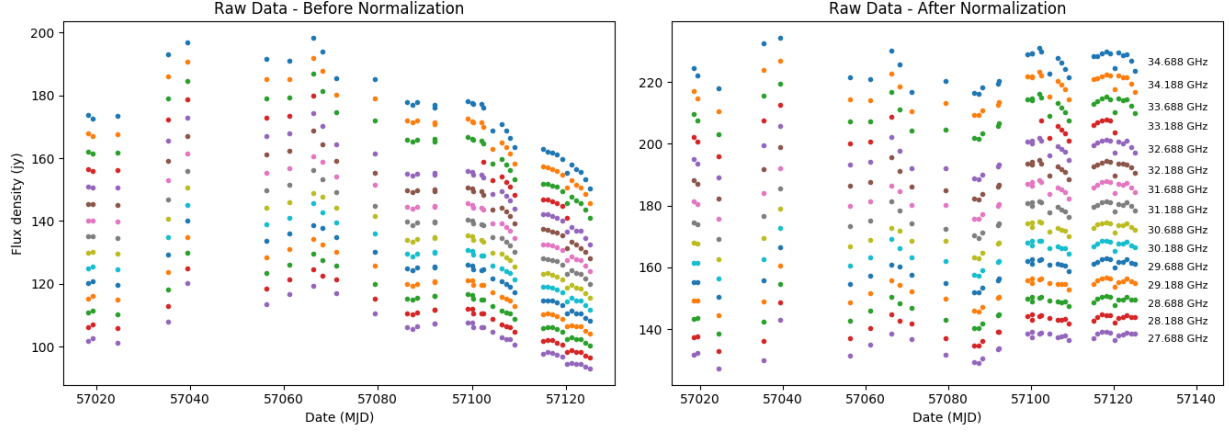
Figure 1: Flux density measurements by time, before and after distance adjustment.
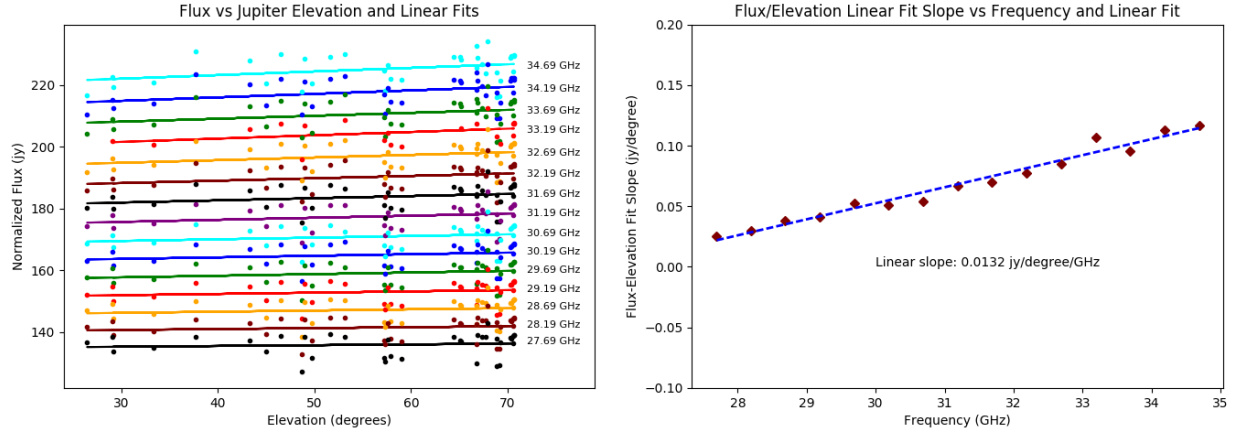

Figure 2: Indication of linear dependence of flux on elevation, and more importantly, linear dependence of flux-elevation slope on frequency.

in the original measurements. The slopes of each channel's correlation are positive linear by frequency and therefore simple to normalize out, as demonstrated in Figure 2, assuming that the measurements taken at higher elevations through thinner layers of atmosphere are more accurate.

The flux densities are averaged across time with weights corresponding inversely to the thermal error on each measurement. Averages are calculated as

$$F_{\nu, meas} = \langle F_\nu \rangle = \frac{\sum_i w_{\nu,i} F_{\nu,i}}{\sum_i w_{\nu,i}}$$

where

$$w_{\nu,i} = 1/\sigma_{\nu,i}^2$$

such that $\sigma_{\nu,i}$ is the stated thermal error in janskys on the ith measurement for a given channel. Averaging the flux densities themselves is fairly straightforward; the rest of this section will discuss the application of meaningful error estimates.

2.1.1 Absolute (σ_A) and Relative (σ_R) Uncertainty

We define two distinct error measurements for the data set: absolute uncertainty σ_A and relative uncertainty σ_R. Absolute uncertainty will quantify our estimate of the calibration accuracy of the SZA and lends the entire ensemble of resulting points a potential vertical offset. The σ_A measurement cannot wildly upset the relationship between points within this set; it is primarily a characteristic of the ensemble as a whole. From COPSS, we quote an estimated upper limit of $< 5\%$ on this calibration error.

3

Meanwhile, relative uncertainty quantifies the stability of each channel with respect to the others, estimating internal consistency rather than absolute accuracy. We know CARMA to exhibit strong spectral stability and can observe this feature in the strongly correlated cross-channel behavior displayed in Figures 1 and 2, which suggests that the σ_R measurement, while allowing some independent uncertainty on points, is expected to be smaller than σ_A and so will not have as great an effect on the overall position of the ensemble. σ_R is useful in defending the use of the relative structure of the ensemble as a comparably reliable tool to the absolute position as well as quantifying a model's match to this relative structure during the model-comparison process. σ_A, by contrast, serves as a more conventional uncertainty estimate.

We approach the absolute uncertainty σ_A estimate using statistical properties of the flux density ensemble along with their stated thermal errors. The statistical contribution $\hat{\sigma}$ dwarfs the thermal contribution $\hat{n}$, but is included for the sake of rigor.

$$\sigma_A(\hat{\sigma}, \hat{n}) = \hat{\sigma}^2 + \hat{n}^2$$

Thermal contribution $\hat{n}$ is calculated as the reciprocal sum of thermal uncertainties for a given channel. With w_i defined above, $\hat{n}$ is defined

$$\frac{1}{\hat{n}^2} = \sum_i w_i$$

Statistical contribution $\hat{\sigma}$, dominating this absolute uncertainty estimate, is calculated as a weighted standard deviation, given w_i as well as the series fluxes $F_{\nu,i}$ and the channel average $\langle F_\nu \rangle$.

$$\hat{\sigma}^2 = \frac{\sum_i w_i \big(F_{\nu,i} - \langle F_\nu \rangle\big)^2}{\sum_i w_i}$$

In this way, we merge statistical 1-sigma error on a channel's flux ensemble with the thermal uncertainty of the points themselves and produce the value σ_A, our estimate of uncertainty on the absolute calibration of the instrument. This we find to be closer to $\sim 2\%$, which falls under the upper limit stated by COPSS.

Relative uncertainty σ_R comprises both thermal contribution as well as the tendency of each channel to deviate from the others. A perfectly stable instrument should exhibit a consistent cross-channel reaction to small, day-to-day variation in observed flux; unexpected behavior should be reflected in σ_R. We compare observations across channels by normalizing each channel with its average.[2] The normalized measurements are denoted $f_{\nu,i}$.

$$f_{\nu,i} = \frac{F_{\nu,i}}{\langle F_{\nu,i} \rangle_\nu}$$

This fraction is averaged across each observation to find the daily mean deviation from each channel's respective average. A stable instrument's channels would exhibit minimal spread around this daily mean deviation, and any spread should be uncorrelated with channel. We isolate the residuals $\delta_{\nu,i}$ from this daily average by subtracting the daily mean deviation from each observation set of normalized measurements, so as to excuse the daily deviation itself but examine each channel's deviation from this deviation. These residuals are defractionalized by multiplying by the channel average.

$$\delta_{\nu,i} = (f_{\nu,i} - \langle f_{\nu,i} \rangle_i) \cdot \langle F_{\nu,i} \rangle_\nu$$

Each channel's behavior is now quantified by its mean deviation from the daily average as well as the spread of these deviations, given by their variance across each channel. During this examination, it was noted that the channels had a tendency to vary together; they often would pivot around the 31.188 GHz measurement, which remained stable to within 0.5% of the measurement value. The frequencies at either extreme (27.688 GHz and 34.688 GHz) varied by no more than 6%. It is unclear what causes this linear variation, but it is worth mentioning that even though this estimate aims to describe the uncertainty of these points relative to each other, it is an overestimate. There remains some unidentifiable cross-channel dependency.

We introduce a thermal component as well, calculated by fractionalizing each thermal error by its accompanying measurement, averaging across each channel, and denormalizing with the channel average.

$$\sigma_{th} = \left\langle \frac{\sigma_i}{F_{\nu,i}} \right\rangle_\nu \langle F_{\nu,i} \rangle_\nu$$

---

[2]Until now, all averages have been across time, isolated to each channel. In this section, that will no longer be the case, so averages will be marked as either channel averages (ν) summed across all observations as before, or "daily" averages (i) calculated with sums across all channels, isolated to each observation.

The final relative uncertainty measurement contains the thermal component σ_{th} as well as the mean $\langle \delta_{\nu,i} \rangle_\nu$ and standard deviation $\left\langle (\delta_{\nu,i} - \langle \delta_{\nu,i} \rangle_\nu)^2 \right\rangle_\nu^{1/2}$ of the daily deviations by channel. The third term, the variance of the channel's daily deviations, dominates the entire measurement and gives each channel a relative uncertainty on the order of a jansky.

$$\sigma_R^2 = \sigma_{th}^2 + \langle \delta_{\nu,i} \rangle_\nu^2 + \left\langle (\delta_{\nu,i} - \langle \delta_{\nu,i} \rangle_\nu)^2 \right\rangle_\nu$$

2.1.2   Synchrotron Correction

With the relatively large SZA beam, covering $\theta_B \approx 11'$ full width at half maximum, we measure Jupiter's total flux density; this comprises both thermal and nonthermal components. In this frequency regime, synchrotron radiation dominates the nonthermal emission. Since we are interested only in the thermal component, we must subtract out the synchrotron radiation from the total observed flux density.

Jupiter's dynamic synchrotron spectrum has been a subject of discussion since the 1970s when a series of observations suggested time variability in the low-frequency[3] spectrum (Klein 1976). A survey of that spectrum from 74 MHz up to 8 GHz, described in de Pater et al. 2003, suggests that synchrotron contribution to the planet's radio spectrum drops off above 2 GHz, so we believe that, with frequencies around 30 GHz, our measurements are fairly safe from significant synchrotron-induced variability. Additionally, Klein 1976 observes that fluctuations on the order of days did not exceed 10%, and explores several-year variability with 1-3 month averages, implying that our 5-month average should capture an approximately constant period of synchrotron variability. Under this assumption, we use a simplified and time-independent model of synchrotron contribution to recover the thermal spectrum. The correction is purely arithmetic and thus does not propagate into uncertainties.

JG uses a value of 1.5 Jy for the synchrotron contribution to a 28.5 GHz measurement of the thermal spectrum, which has a value of about 145 Jy, based on work done by de Pater and Dunn 2003. In order to adjust extant data in the same frequency regime, JG adopts a relationship of $F_{\nu,\,synch} \sim \nu^{-0.4}$, leading to the local model

$$F_{\nu,\,synch} = (1.5\ Jy)\left(\frac{\nu}{28.5\ GHz} \right)^{-0.4}$$

We find this model acceptable across our small frequency domain, especially considering the comparability of the synchrotron contribution to the uncertainty estimates for these data.

The synchrotron model is subtracted from the time-averaged flux density at each channel, yielding thermal-only flux density measurements:

$$F_{\nu,\,thermal} = F_{\nu,\,meas} - F_{\nu,\,synch}$$

2.2   Conversion to Brightness Temperature and Cosmic Microwave Background (CMB) Adjustment

Thermal radiation flux density $F_{\nu\,thermal}$ is converted to brightness temperature T_b via the Planck function. The resulting $T_{b,\,meas}$ from a direct conversion is not yet indicative of the true temperature of the emitter – it is the contrast between the emitter and the microwave background. Correction for this is made during conversion, following a similar adjustment made in de Pater et al. 2014. Observed thermal flux density is set equal to a combination of thermal brightness temperature and CMB contribution by the Planck function, as below, allowing $T_{cmb} = 2.725$ K.

$$F_\nu = \frac{2h\nu^3}{c^2}\left(\frac{1}{e^{\frac{h\nu}{kT_b}} - 1} - \frac{1}{e^{\frac{h\nu}{kT_{cmb}}} - 1} \right)\frac{\pi R_{eq} R_p'}{D^2}$$

where apparent polar radius is given by $R_p' = \sqrt{R_{eq}^2 \sin^2 \phi + R_p^2 \cos^2 \phi}$. Subearth latitude used here is $\phi = 0.15°$, which is the average over a tight cluster of small, similar ϕ values over the four month observation interval according to the JPL Horizons interface.

Working values at each major step as well as final measurements and associated errors are laid out in Table 1. The T_b values, along with some combination of the σ_A and σ_R errors, are appropriate for reproduction in future work.

---

[3]Klein 1976 uses 11-13 cm and 21 cm, considerably longer wavelengths than our 1 cm.

f (GHz)	λ (cm)	$F_{\nu, meas}$ (jy)	$F_{\nu, thermal}$ (jy)	T_b (K)	σ_A (K)	σ_R (K)
34.688	0.864	226.612	225.225	151.013	3.180	1.359
34.188	0.877	219.250	217.855	150.385	3.143	1.186
33.688	0.890	211.832	210.429	149.615	3.222	1.037
33.188	0.903	206.006	204.594	149.876	2.531	1.244
32.688	0.917	198.089	196.669	148.534	3.244	0.620
32.188	0.931	191.047	189.618	147.707	3.228	0.510
31.688	0.946	184.615	183.177	147.235	3.240	0.316
31.188	0.961	178.155	176.708	146.635	3.293	0.146
30.688	0.977	171.458	170.002	145.720	3.266	0.378
30.188	0.993	165.546	164.080	145.347	3.382	0.395
29.688	1.010	159.553	158.077	144.794	3.515	0.675
29.188	1.027	153.335	151.849	143.911	3.584	0.769
28.688	1.045	147.477	145.981	143.225	3.679	0.960
28.188	1.064	141.586	140.080	142.369	3.767	1.147
27.688	1.083	136.081	134.563	141.757	3.875	1.368

Table 1: Values at each frequency through major correction steps, after averaging. $F_{\nu, meas}$ and $F_{\nu, thermal}$ are normalized to 4.04 AU. T_b values include CMB correction. Error estimates are given for the final T_b values only.

2.3 Jackknife Testing

Data are presumably fully processed at this point. In order to ensure that no further identifiable systematics are present, we engage in some brief jackknife tests during which we run arbitrarily selected halves of the time-series data through the analysis pipeline and observe the average resulting change in brightness temperatures. The data are halved both on meaningless criteria, such as odd/even index, as well as by criteria with more systematic potential, such as Jupiter's horizontal elevation at the time of observation.

It was mentioned earlier that what may be an airmass calibration error in the raw data was detected by one of these jackknife tests, specifically one using Jupiter's elevation. After this correction, all subsequent jackknife tests amount to nothing more than noise at less than 2% variation from the full-range values, indicating that we have identified all major systematics about which we have information. The consistency of our measurements with the Gibson and WMAP points corroborates this, or at least suggests that we all suffer from the same unknown systematics.

3 Model Fitting

As briefly discussed in Section 1, the main source of radio opacity in Jupiter's atmosphere is ammonia gas. The following subsections outline our methods for determining NH_3 abundance in the part of the atmosphere to which our measurements are sensitive.

3.1 Nominal NH_3 Profile

Our calculations use the radiative transfer code most recently used in de Pater et al. 2016; this code is based upon an atmosphere in thermochemical equilibrium, as described in detail by de Pater et al. 2005. As in de Pater et al. 2016, we assume for our nominal model that all constituents (NH_3, H_2S, CH_4, and H_2O) are enhanced by a factor of 4.5 above solar in the deep atmosphere ($P > 8$ bar), as observed by the Galileo probe for NH_3, H_2S, and CH_4 (Folkner et al. 1998, Mahaffy et al. 1999, Sromovsky et al. 1998, Wong et al. 2004). At higher altitudes, NH_3 will be partially dissolved in the water cloud (~ 6 bar), will form the NH_4SH cloud (~ 2.5 bar), and at $P < \sim 0.8$ bar will condense into its own ice cloud and follow the saturated vapor curve. In our nominal model we thus assume an NH_3 abundance of 5.72×10^{-4} in Jupiter's deep atmosphere, which is diminished at altitudes at which clouds form. We adopt a 100% humidity within and above the NH_3 ice cloud in our nominal model. This results in a constant abundance of 1.20×10^{-7} near and above tropopause.
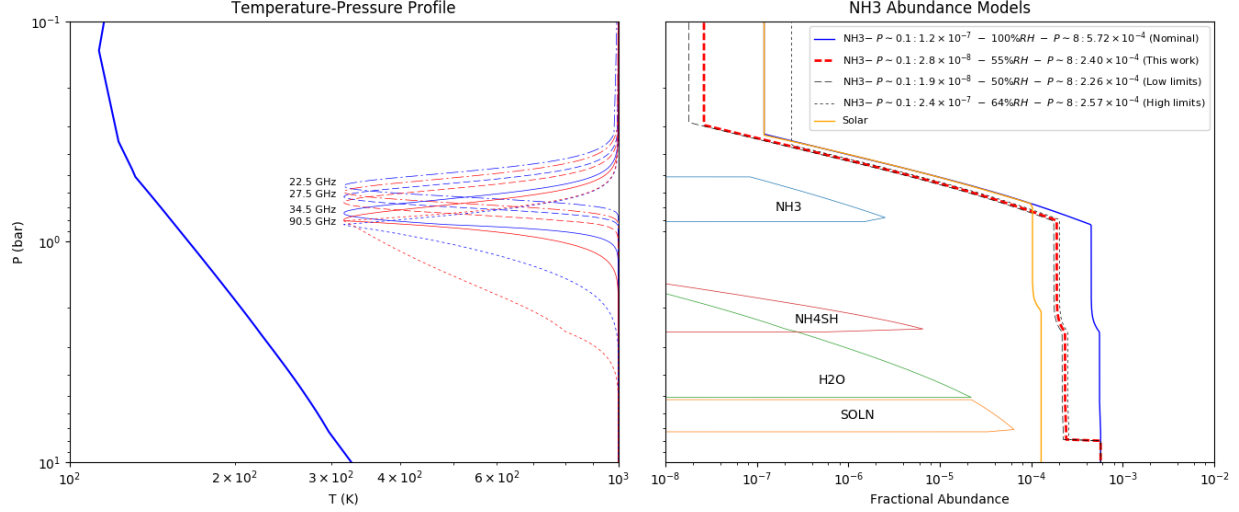
Figure 3: On the left, the temperature-pressure profile used in our model of Jupiter's atmosphere. Several weighting functions are overlaid on the right edge of this figure. On the right, the fractional NH$_3$ abundances according to the solar and nominal constituent abundance models plotted next to three selected models. The red dashed line indicates the abundance model that agrees best with the measurements using our 3-parameter grid fit, and the thinner black lines indicate global high- and low-abundance limits using the error bounds for each parameter. The lower bound for high atmosphere abundance is not certain; this plot uses the small value resulting from the Clausius-Clapeyron equation of state. Cloud levels are overlaid on the left hand side of this panel.

3.2   Model Generation Through Perturbation

Starting with the nominal NH3 abundance profile described above, we apply to it small, unity-order adjustments, which in turn gives us the ability to generate a range of theoretical emission profiles. These theoretical profiles are compared to the available measurements in order to isolate an abundance profile in maximal agreement with observational evidence. The profiles are generated using a radiative transfer software, pyplanet, described in de Pater et al. 2014 for its use on Neptune's atmosphere. The software ignores potential opacities from clouds.

We begin this process by separating the atmosphere into regions of altitude based on their radiative contribution to our measurements, according to the nominal NH$_3$ abundance model. These contribution functions, shown on the left panel of Figure 3, are most prevalent between $0.5 < P < 0.8$ bar. This layer coincides with the NH3 ice cloud-forming region, during which NH3 follows the saturated vapor curve, as indicated by the nominal abundance profile shown on the right panel of Figure 3. We apply to this region, defined by its plummeting NH$_3$ abundance, a constant humidity multiplier RH. Through this parameter, we will tune humidity in the cloud-forming region to fit observations.

We similarly treat the regions of constant NH$_3$ abundance above and below this layer, granting them their own modifying constants. The sub-cloud region, defined as the region of approximately constant NH$_3$ abundance between the NH$_3$ cloud and $P < 8$ bar, is modified by the parameter α_d. As we are not sensitive to anything below $P > 8$ bar, we jump the abundance below this point back to the nominal model, which is motivated by Galileo measurements sensitive to this deeper region. The region of constant abundance above tropopause is modified by the parameter α_h.

These parameters, RH, α_d, and α_h, form a three-parameter grid across which we create slightly modified versions of the nominal abundance model. Each element of the grid is run through the radiative transfer software to generate a theoretical emission profile, and each of these profiles is compared to the emission measurements such that each point on the three-dimensional grid is associated with a χ^2 value. We search the parameter space, bound by a physically reasonable range of unity-order constants, for a global minimum. This minimum is explored to within 0.5% resolution of the nominal value. The abundance profile associated with this minimum is taken to be the profile in maximal agreement with observational evidence. Uncertainty for each parameter is approximated as the region in which the local χ^2 value is less than 2× the minimum χ^2 value.

4   Results

Our 15 SZA measurements of Jupiter's atmospheric thermal emission show a smoothly sloped sample of the shorter-wavelength side of the 1.3 cm NH_3 absorption band. We compare them with the surrounding WMAP and Klein & Gulkis sets as adjusted in JG as well as Gibson's original point at 28.5 GHz, and updated VLA measurements from de Pater et al. 2016. The SZA observations are consistent to well within 1% with points from these existing measurements that fall between 27-35 GHz.

We implement the model-measurement comparison scheme discussed in the previous section and generate a grid of theoretical emission profiles and corresponding χ^2 comparison results.

4.1   Sub-Cloud Abundance α_d

We examine NH_3 abundance below the cloud-forming region relative to the nominal abundance value of 5.72×10^{-4}. The model comparison process indicates a value of 2.40×10^{-4}, with uncertainty bounding it between $[2.26, 2.57] \times 10^{-4}$. This value produces a predicted emission profile that agrees well with all observations, especially the high frequency WMAP points most sensitive to the deeper atmosphere.

4.2   Relative Humidity RH

Humidity is examined relative to the saturation curve region in the nominal model, roughly between $0.3 < P < 0.8$ bar. The nominal model follows 100% humidity, so our results will be considered relative to a fully saturated model. Results of the comparison process suggest a humidity of 56.5%, bounded between $[50\%, 63.5\%]$. This humidity adjustment produces models that are consistent with all observations, especially the lower frequency CARMA points, the Gibson point that are most sensitive to this pressure range.

JG states that NH_3 abundance is, on average, subsaturated by at least a factor of 2 at $P < 0.6$ bar. Our results corroborate this subsaturation, within our own pressure regime stated above, down to the factor of 2, but add a tighter bound based on 4 independent sets of measurements.

4.3   High Atmosphere Abundance α_h

High atmosphere abundance is examined relative to the nominal value of 1.2×10^{-7}. The comparison process suggests a value of about 2.8×10^{-8}, nearly one fifth of the original, but yields an upper bound of 2.4×10^{-7}, twice the original value. Since we are not very sensitive to these pressures, we are not able to provide a lower bound.

This result relies primarily on the lowest frequency WMAP measurement but has some input from the lower frequency CARMA measurements. It is difficult to place any reasonable bound on the high atmosphere abundance due to the lack of data near the band center; the Klein & Gulkis measurements were deemed to uncertain for our comparison, but all tend toward temperatures higher than the WMAP point. Higher temperature at the band center would indicate a lower pressure departure from the saturation curve and consequently a smaller high atmosphere abundance. The precise number found in our analysis is likely meaningless – nevertheless, it is quite possible that the high atmosphere abundance should be smaller than its value in the nominal model.

5   Conclusion

We began with 37 secondary calibration scans of Jupiter over the course of 5 months, made with CARMA at 15 different frequencies between 27-35 GHz. From there, we reduced this into 15 measurements of Jupiter's thermal brightness, limited to the case of the disk-averaged atmosphere. With these data, we filled in a ~ 10 GHz wide section of Jupiter's thermal emission profile, near an NH_3 absorption band. CARMA's strong spectral stability lends our data a strong certainty in slope, so we used this slope measurement as well as our absolute calibration, to some degree, and several surrounding data to better characterize the band shape. We modeled to this band shape by designing a model-comparison process around a radiative transfer code and found that, compared to the nominal abundance value, our characterization of the band shape suggests a globally lower abundance, to varying degrees at three distinct pressure regions in the atmosphere. Deep atmosphere abundance between $P < 8$ bar and the $P \sim 0.8$ bar condensation point is found to be 2.40×10^{-4}, bounded between $[2.26, 2.57] \times 10^{-4}$. Relative humidity, within the NH_3 cloud layer where abundance follows the saturation curve, is found to be 56.5%,
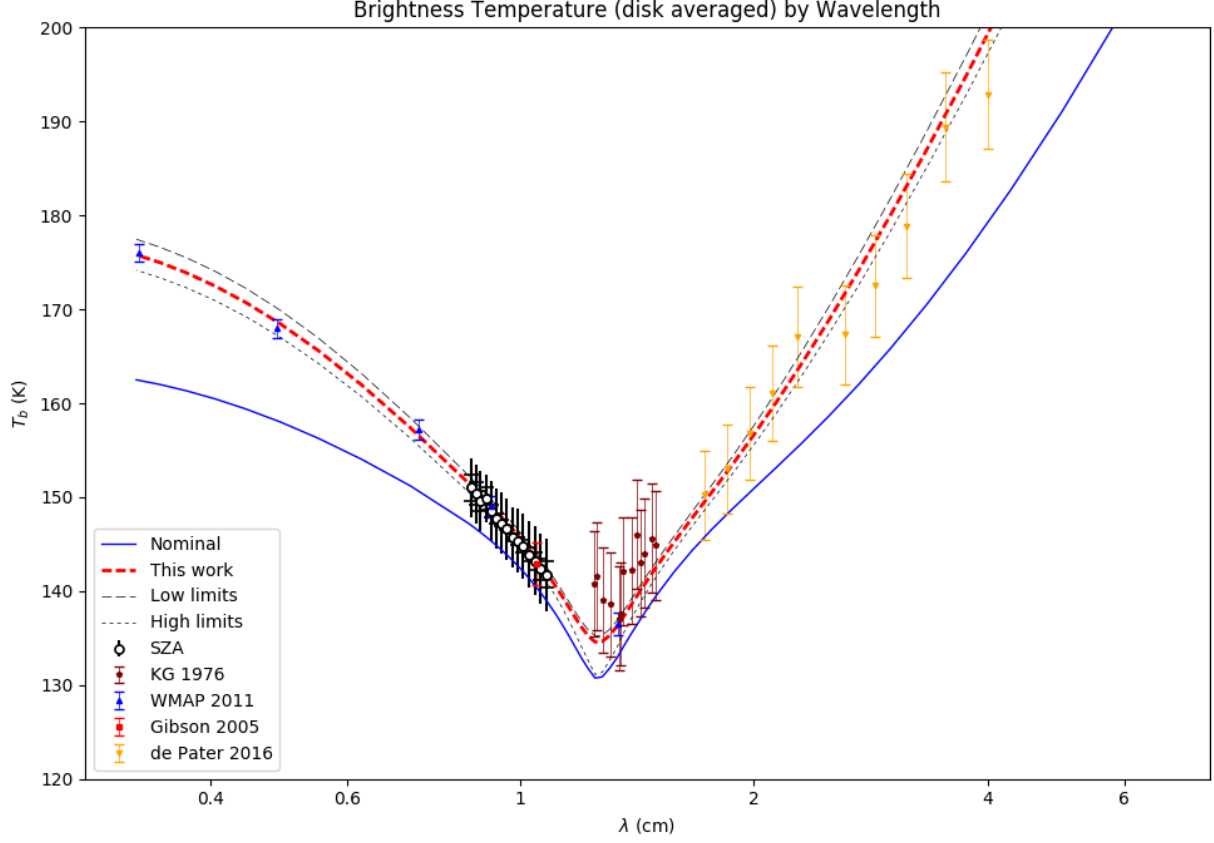
Figure 4: CARMA measurements of disk-averaged brightness temperature together with extant measurements. Nominal model is included, as well as the model we suggest in this work, using parameters discussed in Section 4, and the global high- and low-abundance limits. The lower limit for high atmospheric abundance is, as discussed in the text, not stated in this work. CARMA measurements are shown with relative certainty at the capped error bars and absolute uncertainty at the larger, uncapped bars. Note the uniformity in absolute certainty and the frequency-dependent variation in relative uncertainty.
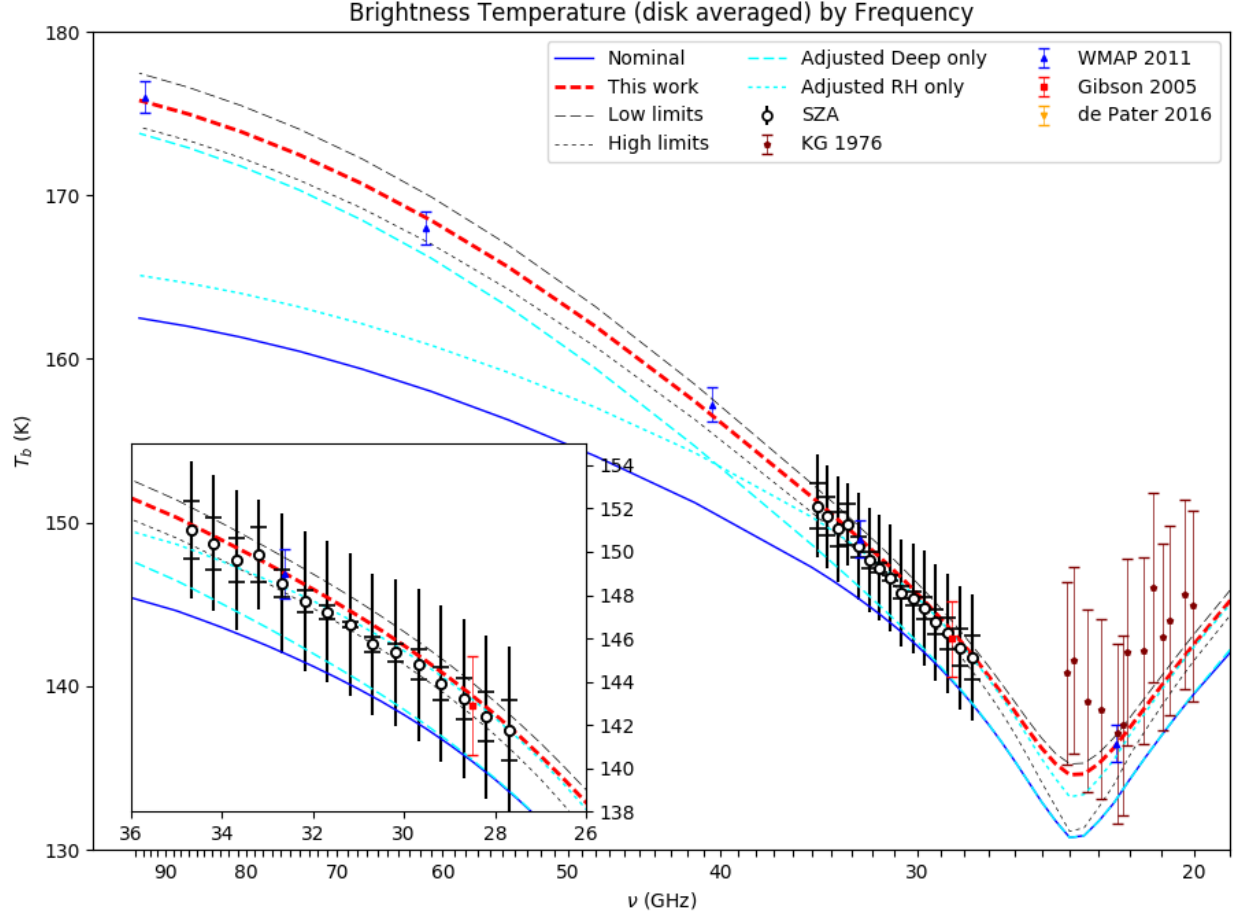
Figure 5: Similar to Figure 5, but restricted to a smaller spectral range and set against a frequency axis. Inset panel provides a clearer view of the CARMA points reduced in this work. We include two additional models, indicated by cyan lines, representing one-parameter deviations from the nominal model; in other words, we hold two parameters at 100% of the nominal value and let the third take on the preferred value based on the χ^2 fit so as to demonstrate the effects of the parameters as well as their general independence to each other. The effects of relative humidity and deep atmosphere abundance are shown by the two cyan lines. High atmosphere abundance is not shown here, but when decreased raises the temperature at the band center and accounts for the band center difference between the relative-humidity-only and preferred (red-dashed) models.

bounded between $[50\%, 63.5\%]$. Top atmosphere abundance, above the NH$_3$ cloud layer and past the departure from the saturation curve, is found to have an upper bound of 2.4×10^{-7}, but is indicated through two separate analysis methods to be closer to 2×10^{-8}. These results seem to echo the conclusion made in JG, especially that of subsaturation by a factor of 2.

We hope that this measurement set will be useful in future explorations, as have WMAP, Gibson, and others been in ours. These results are of course limited to the case of the disk-averaged atmosphere, and we look forward to ongoing and future projects who will expand this research to the spatially resolved case. We look forward to the release of data from the Juno probe mission in particular; while its investigation will involve some spatial resolution, it may serve to confirm or correct our findings.

CARMA's calibration is strong enough that we feel these reduced thermal measurements may be useful as calibration information for interferometers lacking short baselines. The measurements produced in this work are believed to encompass all flux from the disk, so they may be treated as "single-dish" flux measurements to give calibration context to interferometer scans.

6 References

1. de Pater 1990 (synch low wl)
2. de Pater et al. 2003
3. de Pater et al. 2014
4. de Pater et al. 2016
5. Gibson et al. 2005
6. Klein 1976
7. Keating et al. 2016
8. Thornton and Welch 1963
9. Weiland et al. 2011
10. Wildt 1937 (first ammonia)

References